Reduced graphene oxide/silver nanohybrid as a multifunctional material for antibacterial, anticancer, and SERS applications

Priya Parvathi Ameena Jose[1] · M. S. Kala[1] · Alphonsa Vijaya Joseph[2] · Nandakumar Kalarikkal[3] · Sabu Thomas[3]

Abstract

Development of multipurpose materials like graphene–silver hybrid nanocomposite has attracted much appreciation in recent years because of their improved synergistic properties like higher effective surface area, high electron mobility, stability, and biocompatibility. Here, we report the synthesis, characterization, and multifunctional properties of reduced graphene oxide/silver (rGO/Ag) nanohybrid. This novel material shows promising results against two antibiotic resistant bacteria—Escherichia coli and Bacillus subtilis. The toxicity study on Gram-negative bacteria (*Escherichia coli*) and Gram-positive bacteria (*Bacillus subtilis*) was done by the evaluation of cell viability through Resazurin-based Microtitre Dilution Assay (RMDA). We have observed that this nanohybrid is more effective against *Bacillus subtilis* than *Escherichia coli* which is different from the conventional observations. With Dalton's Lymphoma Ascites cells (DLA), we have examined short-term in vitro cytotoxicity of this nanohybrid by trypan blue dye exclusion technique. The anticancer response of this nanohybrid was recorded with Human Colon epithelial carcinoma cells (HCT-15) as well by MTT assay. We also report SERS effect of (rGO/Ag) substrate in detecting very small amounts of Rhodamine B molecules by estimating the analytical enhancement factor.

Keywords Graphene oxide · Silver nanoparticle · Nano hybrid · Antibacterial activity · Cytotoxicity · SERS

1 Introduction

For a long time, nanomaterials, especially metal nanostructures, have attracted much attention from researchers due to its versatility in applications. Among various metal nanostructures, silver nanostructures have acquired great regard because of the broad-spectrum antimicrobial effects of silver which were well known from ancient times [1–3]. The interesting and promising chemical, biological, and physical properties of silver nanostructures made them suitable candidates for various biomedical applications [4–9]. Recently, silver nanoparticles (AgNP) have also extended their sanative power to cancer care area [10–12]. Several in vitro studies with silver nanoparticles have emphasized their potentiality as an effective anticancer agent [13–18]. Another area in which AgNPs have achieved great momentum is in the field of surface enhanced Raman spectroscopy (SERS) which is a consequence of its unique nanosize property called localized surface plasmon resonance (LSPR) [19–22]. The large SERS enhancement ability of AgNPs makes them good detection platforms for SERS signals. Literature studies have indicated that performance and applicability of AgNPs in all these diverse fields strongly depend upon their size, shape, and distribution [23]. However, the prospects of application of the nanoparticles become limited due to various reasons. During the preparation process, these nanoparticles tend to aggregate to minimize their surface area and thereby surface energy, which in turn causes bewildering deterioration of their properties. Easy oxidation of these particles is another reason for their poor performance. To solve these problems, it is essential to find a proper method for the growth and stabilization of silver nanoparticles. Loading of nanoparticles on proper supporting matrices like graphene-based materials is one of the strategies widely applied to overcome these

✉ M. S. Kala
kalams@teresas.ac.in

[1] Department of Physics, St.Teresa's College, Ernakulam, Kerala, India

[2] Department of Botany, St.Teresa's College, Ernakulam, Kerala, India

[3] International and Inter University Centre for Nanoscience and Nanotechnology, M G University, Kottayam, Kerala, India

shortcomings [24]. Due to their unique physical, thermal, mechanical, and tunable chemical properties, graphene materials have emerged as an excellent supporting material for nanoparticles.

Graphene oxide (GO) is a planar sheet of single /few layer sp^2 hybridized carbon atoms with easily reducible oxygen functional groups such as hydroxyl and epoxy on the basal plane and carbonyl and carboxyl at the edges of the sheet. The presence of all these oxygen functional groups imparts hydrophilic property to GO which easily allows the growth of metallic nanoparticles. Furthermore, GO has unique properties including large surface area, low cytotoxicity, and good water stability [23]. All these factors help GO to act as a platform for the growth and stabilization of metal particles and subsequently succeed into its realization in various application fields [25]. Biocompatibility, size, and shape depending tunable properties and functionalities make GO the most promising functional material used in various applications [26]. The unique features such as featured structure, interesting physiochemical properties, and other characteristics like oxidative stress effect, cell entrapment ability, and edge cutting effect make GO as one of the most effective antibacterial nanomaterials in the world [27].

Recently, many researchers have reported the superior performance of graphene oxide (GO) and reduced graphene oxide (rGO) as antimicrobial and anticancerous agents which enhance their potential usage in biomedical areas [28–35]. In addition, the properties like chemical enhancement, molecular enrichment, fluorescence quenching, and high adsorption to target molecules exhibited by graphene and related materials make them promising substances in fabricating advanced SERS substrates for sensitive detection of various molecules including biomolecules [36–40].

In this work, we report the synthesis of reduced GO decorated with silver nanoparticles–rGO/Ag nanohybrid and its multifunctional performance in the areas of antibacterial and anticancerous activity and SERS enhancement. To check its antibacterial activity, we have followed Resazurin-based Microtiter Dilution Assay (RMDA) method with two bacterial strains. We also performed in vitro cytotoxicity experiments with Dalton's Lymphoma Ascites cells (DLA) and Human Colon epithelial carcinoma cells (HCT-15) to verify the possibility of using this hybrid as a clinically active chemotherapy agent in nanomedicine. We hope that this study may impart a new perception for the better evaluation of antibacterial and anticancer actions of (rGO)-Ag nanohybrids which is beneficial for the applications in biomedical and other related fields. We have also investigated the capability of this material as an SERS substrate using Rhodamine B as the probe molecule. Our experimental outcome displays that this SERS substrate has excellent sensitivity for the detection of Rhodamine B with admirable reproducibility.

2 Materials and methods

2.1 Materials

Graphite flakes (98%, 60 mesh), sodium nitrate, concentrated sulphuric acid (98%), potassium permanganate, hydrogen peroxide (30%), hydrochloric acid (98%), silver nitrate, trisodium citrate, sodium borohydride, and Resazurin were purchased from Merck India. Dimethyl sulfoxide (DMSO), 3-(4,5-dimethylthiazol-2-yl)-2,5-diphenyltetrazolium Bromide (MTT) reagent, and Trypan blue were procured from Sigma-Aldrich. All these chemicals were of analytical grade and used without any further purification.

The Dalton's Lymphoma Ascites (DLA) cells were maintained in vivo in Swiss albino mice by intraperitoneal transplantation. Freshly aspired cells from the peritoneal cavity of tumour bearing mouse were washed thrice with phosphate-buffered saline (PBS) under sterile conditions. The cell count was done and further dilutions were made, so that the concentration was maintained as 10^6 cells in 0.1 mL.

Human Colon epithelial carcinoma cells (HCT-15) (Passage number 30) were procured from National Centre for Cell Sciences, Pune, India, and maintained in RPMI-1640 media, supplemented with 10% fetal bovine serum, 100 U/mL penicillin, and 100 μg/mL streptomycin, and kept at 37 ℃ in an incubator with 5% CO_2. The cells were passaged at 80% confluency and medium was changed every third day.

2.2 Synthesis of reduced graphene oxide decorated with silver nanoparticles

GO (AF) was prepared from graphite flakes by modified Hummer's method [41]. To 10 mL of GO uniform solution (0.6 mg/mL), $AgNO_3$ (0.2 M) solution was added gradually, followed by the sudden addition of trisodium citrate solution (0.2 M). After continuing the stirring for 30 min, 0.2 M $NaBH_4$ solution was dropped slowly at room temperature to this mixture. Stirring was continued for five more hours and the final product—silver anchored on reduced graphene oxide nanohybrid (AGS) was filtered, washed, and dried in hot air oven at 50 ℃ for 4 h [42]. Pure silver nanoparticles (AS) were also prepared in the same manner by replacing GO solution with distilled water.

2.3 Characterization

The structure and composition of the samples were characterized by X-ray powder diffractometer (Bruker AXS D8 Advance). The diffuse reflection spectra of the samples were recorded with Varian, Cary5000 UV–Vis–NIR spectrophotometer, while Thermo Scientific Evolution 201

spectrophotometer was employed to obtain the UV–Vis spectrum from GO. Detection of the chemical functional groups of the samples was done by Fourier transform infrared analysis (Thermo Nicolet, Avatar 370). Raman spectra were acquired using a confocal microprobe Raman system (WITec alpha300RA) with an excitation wavelength of 532 nm from a He–Ne laser. The zeta-potential analysis of the samples was done at 25 °C using Horiba Scientific nanopartica instrument (Nanoparticle Analyzer, SZ-100). To determine the thermal properties, thermogravimetric analysis was carried out with Perkin Elmer, Diamond TG/DTA. Energy-Dispersive X-ray Spectroscopy analysis of the samples was carried out with the EDS (Oxford Instruments) attached with SEM (JEOL Model JSM—6390LV). X-ray photoemission spectroscopy (XPS) data were taken with Auger Electron Spectroscopy (AES) module and C60 sputter gun. The Brunauer–Emmett–Teller (BET) specific surface area of the samples was estimated by nitrogen adsorption–desorption isotherm measurements obtained with a surface area analyzer (Tristar 3000-BET). Morphological features of the samples and the calculation of average size of silver nanoparticles were obtained from transmission electron microscopy with HRTEM- Jeol /JEM 2100 instrument.

2.4 Antibacterial study: minimum inhibitory concentration (MIC) determination by RMDA method

The minimum inhibitory concentration is defined as the minimum amount of the sample needed to show bacteriostatic effect [43]. It is the lowermost concentration of antimicrobial agent that completely inhibits visible growth of the microorganism in microtitre plate as detected visually after a period of incubation [44]. The MIC of the as-prepared samples (AF, AS, and AGS) were measured by Resazurin-based Microtitre Dilution Assay (RMDA). The antibacterial action of the prepared samples (AF, AS, and AGS) were tested against two bacterial strains—*Escherichia coli* (ATCC 8739), the Gram-negative bacteria and *Bacillus subtilis* (ATCC 11778), the Gram-positive bacteria, maintained on nutrient broth. We have prepared the bacterial culture to a final concentration of 10^6 U/mL as reported in the literature [45].

Resazurin is an oxidation–reduction indicator used for the evaluation of cell viability and bacterial contamination, particularly in various cytotoxicity assays [46]. It is a purple non-fluorescent and non-toxic dye which becomes pink and fluorescent when reduced to resorufin by oxidoreductases within viable cells.

Homogeneous solution of resazurin dye was prepared by dissolving 0.032 g in 5 ml sterile water, that of antibiotic by dissolving 0.01 g in 1 mL sterile water and the homogeneous solutions of samples (AF, AS, and AGS) by dissolving 5 mg in 1 mL DMSO. Under aseptic conditions, microtitre plates were used for RMDA. 100 µL of sample materials in 10% (v/v) DMSO was taken in the first row of microtiter plate followed by the filling of 100 µL of nutrient broth. Twofold serial dilution (throughout the column) was attained by removing and placing 100 µL sample material from first row to the successive wells in the next row of the same column, so that each well has 100 µL of sample material in serially descending concentrations. Finally, a volume of 10 µL was taken from bacterial suspension and was added to each well to achieve a final concentration of 10^6 CFU/mL. In this manner, three columns of the microtitre plate were filled with the three sample materials. Each microtitre plate had a set of three controls: (a) C_1—a column with Ampicillin—a broad-spectrum antibiotic as positive control, (b) C_2—a column with nutrient broth and bacteria solutions as negative control, and (c) C_3—a column with all solutions with the exception of the bacterial solution, but adding 10 µL of nutrient broth instead which act as broth control. The microtitre plates were prepared in triplicate and placed in a temperature controlled incubator at 37 °C for 24 h. To avoid the dehydration of bacterial culture, each plate was wrapped loosely with a cling film. After 24 h of incubation, 10 µL of resazurin solution as indicator was added to all 96 wells in the plate. Again, the plates were incubated for 18 h. The colour change was then appraised visually and any colour change from purple to pink was recorded as positive. The lowest concentration of samples at which colour change occurred was taken as the MIC value. The average of three values was calculated and recorded as the MIC for that test sample and the bacterial strain.

2.5 In vitro cytotoxicity studies

To investigate the therapeutic effects of newly synthesized materials, cell viability tests are considered as most suitable. Examining the material's safety to host cell or its cytotoxic effect in cancer cell is very important in such studies. Nowadays, many simple as well as complex methods are available to execute such tests. Exposure of cell to trypan blue is a simple method usually performed to identify the viable cell (unstained) using a microscope [47]. This method is based on the cell membrane permeability. MTT assay is another common method used for the assessment of cell viability and cytotoxicity based on enzyme activity. This assay is a colorimetric one which detects living, not dead cells and the signal generated is dependent on the degree of activation of the cells. Its simplicity and effectiveness make this assay a suitable one to assess the anti-inflammatory and anticancer activities of any test samples at preliminary levels [48].

The anticancer response of the prepared samples was recorded with Dalton's Lymphoma Ascites cells (DLA) by trypan blue dye exclusion technique and Human Colon epithelial carcinoma cells (HCT-15) by MTT assay. This part of the

work has been carried out in Amala Cancer Research Centre, Thrissur, Kerala, India.

2.6 *Short-term* in vitro *cytotoxic analysis by trypan blue assay*

Trypan blue staining is usually considered as a convenient assay for quantitating cell death following treatment with any cytotoxic stimuli [49]. The viable cell suspension (1×10^6 cells in 0.1 mL) was added to tubes containing various concentrations of the test samples and the volume was made up to 1 mL using PBS. These assay mixtures were incubated for 3 h at 37 °C, and then, 1 mL of trypan blue was added. Using a haemocytometer, the number of live cells (unstained) and dead cells (stained) was counted separately from which the percentage of dead cells was calculated using the following equation:

$$\% \text{ of dead cells} = \frac{\text{No. of dead cells}}{\text{No. of live cells} + \text{No. of dead cells}} \times 100. \tag{1}$$

2.7 Long term in vitro cytotoxic analysis by MTT assay

Cytotoxicity study of the prepared samples (AS and AGS) was done on HCT-15 cells using the conventional MTT (3-(4, 5-dimethylthiazol-2-yl)-2,5-diphenyltetrazolium Bromide) assay. The MTT reagent yields low background absorbance values in the absence of cells. The healthy and rapidly growing cells exhibit high rates of MTT reduction to formazan, while the dead or inactive cells fail to do so. The final product of MTT reduction is a purple color formazan that can be easily dissolved in DMSO.

Approximately 1×10^5 /mL cells were seeded in a 24-well plate with complete growth medium (RPMI-1640) and allowed to adhere at 37 °C for 48 h. At 80% confluency, the medium was replaced with fresh media and different concentrations of the samples were added to each well (0–75 μg/mL). The cells were further incubated for 48 h, and at the end of incubation period, the medium was again replaced with fresh one. Then, 50 μL of 0.5% MTT were added to each well and incubated for 4 h. The formazan crystals formed were dissolved in dimethyl sulfoxide and the absorbance was measured at 570 nm in UV/Vis spectrophotometer (Systronics, India). The medium without samples was served as control and triplicate was maintained for all concentrations. The quantitative analysis of cytotoxicity was done based on percentage of dead cells, employing the following equation:

$$\% \text{ cell death} = \frac{\text{Ab}_{\text{control}} - \text{Ab}_{\text{sample}}}{\text{Ab}_{\text{control}}} \times 100. \tag{2}$$

2.8 SERS measurements

SERS spectra were recorded by a confocal Raman spectrometer (WITec instrument) equipped with 532 nm laser and $100 \times$ objective (NA = 0.9). The data acquisition time for each measurement was set as 5 s and the diameter of laser beam spot was 1 μm, while the laser power on the samples was typically in the order of 60 mW. Rhodamine B (RhB) was chosen as the model probe molecule (analyte) for SERS measurements. To prepare SERS active substrates, 20 μL of as-prepared samples (AS and AGS) were incubated with 10 μL of analyte solutions (10^{-3}) for 2 h at room temperature and subsequently deposited on a microscopic glass slide (area ~ 1 cm^2) and dried naturally. By serial dilution method, different concentrations of the analyte were prepared to detect the SERS sensitivity of substrate. To ensure the reproducibility and validate the stability of the substrate, measurements were repeated at different positions.

3 Results and discussion

3.1 Structural and morphological characterizations

Crystalline nature of all samples is revealed by XRD patterns. In Fig. 1a, the characteristic diffraction peak of exfoliated GO appears at $2\theta = 10.7°$ (001 plane) with a large interplanar d-spacing of 8.22 Å which can be assigned to the presence of intercalated oxygen containing functional groups and interlamellar water molecules trapped between adjacent hydrophilic graphene oxide layers [50, 51]. The less intense peak at $2\theta = 42.1°$ commonly observed in
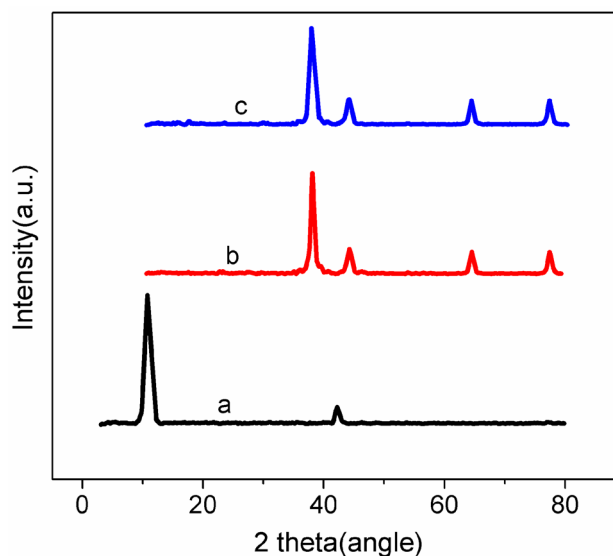

Fig. 1 XRD patterns of **a** graphene oxide, **b** silver nanoparticles, and **c** reduced graphene oxide-silver nanohybrid

graphitic substances indicates the presence of some unexfoliated graphite particles [52]. In Fig. 1b, the distinctive peaks detected at 38.5°, 44.3°, 64.5°, and 77.6° can be assigned to (111), (200), (220), and (311) crystal planes of metallic silver, respectively (ICDD No. 00-004-0783). This establishes the formation of face-centered cubic silver in sample AS. In the hybrid AGS (Fig. 1c), the prominent sharp peaks observed at 37.9°, 44.2°, 64.5°, and 77.5° indicate the successful formation of metal silver in the hybrids. Furthermore, no obvious peaks of graphene oxide/reduced graphene oxide were observed in the as-synthesized AGS hybrid. This might be due to the relatively lower content of graphene oxide and/or might be due to the strong diffraction signals of silver suppressing those of graphene oxide sheets [53]. Another possibility is the complete exfoliation of GO [54]. The loading of AgNPs on the surface of the GO sheets might have averted the restacking of the layered structure of GO [55].

UV–visible absorption spectrum of AF (Fig. 2a) exhibits a strong absorption peak at 230 nm owing to the π–π^* transitions of aromatic C–C bonds and a shoulder peak at 300 nm in view of the n–π^* transitions of C=O [56]. The UV analyses of both samples AS and AGS reveal the normal surface plasmon resonance (SPR) peaks at 398 nm and 404 nm, respectively (Fig. 2b) [57]. The sharp symmetric peak of AS at 398 nm suggests the formation of monodispered spherical silver particles without any anisotropic features, while for AGS, the presence of broad peak at 404 nm implies the formation of irregular-shaped polydispersed silver particles of varying size [58].

FTIR spectra shown in Fig. 3 indicate the nature of the chemical functionalities present in AF and AGS samples. The characteristic vibrations of GO observed in AF are represented by the peaks appearing at 3388 cm^{-1} (OH-stretching vibration), 1721 cm^{-1} (symmetric stretching vibration of carboxyl C=O group), 1400 cm^{-1} (C–OH), 1222 cm^{-1} (C–OH stretching), and 1050 cm^{-1} (C–O-stretching vibration) [59]. All these oxygen containing groups denote the efficient oxidation process of graphite flakes. The peak observed in AF at 1620 cm^{-1} is possibly due to the presence of (O–C=O), (C=O), and (OH bending) functional groups, while those at 2822 cm^{-1} and 2896 cm^{-1} are assumed to be due to C–H-stretching adjacent to –COO group [60]. The FTIR measurements of AGS suggest the interaction between GO and silver nanoparticles which causes a change in peak positions. The (C–O-stretching vibration) observed at 1050 cm^{-1} is shifted to 1025 cm^{-1} with reduction in intensity. The peaks appeared at 1400 cm^{-1} and 1620 cm^{-1} are also displaced to 1388 cm^{-1} and 1592 cm^{-1} with decreased intensity. The peaks observed at 1222 cm^{-1}, 1721 cm^{-1}, 2822 cm^{-1}, and 2896 cm^{-1} are missing in the FTIR spectrum of AGS. The disappearance or decrease in intensity of these peaks
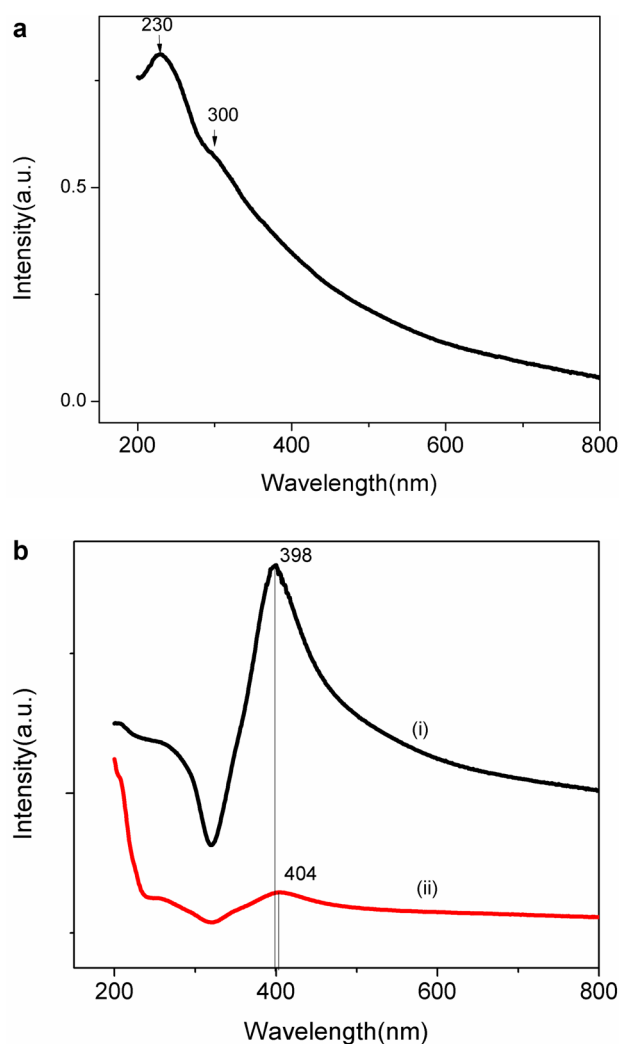
Fig. 2 a UV–visible absorption spectra of graphene oxide. **b** DRS spectra of (i) graphene oxide and (ii) reduced graphene oxide–silver nanohybrid

representing oxygen containing groups implies the partial reduction of graphene oxide in the AGS sample [61].

Raman spectroscopy, a powerful high-resolution technique, provides the much needed swift and simple structural and quality characterization of graphitic materials. The spectrum of AF (Fig. 4) has two prominent peaks, the G band around 1585 cm^{-1} caused by the Raman active phonon (in-plane optical mode) close to the Γ point and the D band around 1350 cm^{-1} whose signal strength depends strongly on the amount of disorder in the graphitic material [62]. Due to the surface enhanced scattering of Ag NPs, an increase in intensities of D and G bands is in AGS [63]. In addition to these, two more bands—the overtone of the D band (2D) at about 2700 cm^{-1} and the disorder induced D + G combination mode at about 2950 cm^{-1}—are also distinguishable in AGS (shown in inset c of Fig. 4) [64].
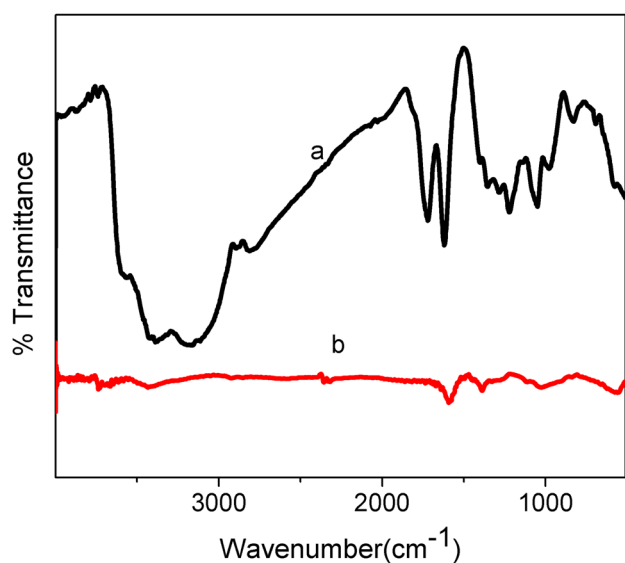
Fig. 3 FTIR spectra of **a** graphene oxide and **b** reduced graphene oxide–silver nanohybrid
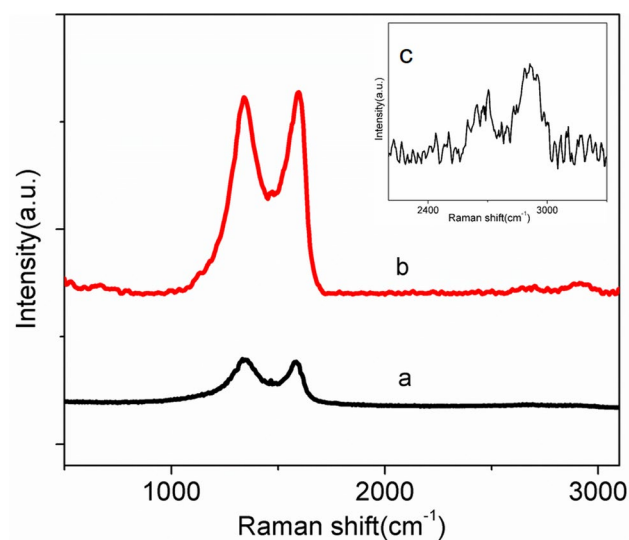

Fig. 4 Raman spectra of **a** graphene oxide, **b** reduced graphene oxide–silver nanohybrid, and **c** 2D and (D + G) bands of reduced graphene oxide–silver nanohybrid

Zeta potential is a fundamental parameter used to quantify the surface charge and it is also perceived to affect the stability of colloidal nanomaterials [65, 66]. The surface charge measured by zeta potential is shown in Fig. 5. The negative zeta-potential value of AF (− 39 mV) indicates the presence of large numbers of carboxyl and epoxy groups with a high density of negative charge in GO sheets [67]. Silver nanoparticles in aqueous medium showed a comparatively higher value of − 55 mV, whereas that of AGS showed a higher negative zeta-potential value of

− 60 mV indicating the greater stability and suspensibility of nano hybrid [68].

Thermal stability of synthesized samples was carried out by thermogravimetric analysis and the results are shown in Fig. 6. The TGA curve of AF shows a weight loss of about 10% below 140 ℃ which may be due to the removal of residually adsorbed and combined water, which resides in the spaces between the GO layers [69]. Another noticeable weight loss (10%) observed between (140–202 ℃) range may be due to the pyrolysis of the thermally labile oxygen functionalities such as CO, CO_2, and H_2O vapour [70]. This process continues at a slow rate until at 202 ℃ where a drastic change transpires. More than 75% weight loss that occurs beyond 202 ℃ is due to the decomposition of carbon backbone of graphene sheets [71]. For AS, the weight loss is less than 5% for the entire temperature range which can be attributed to the water molecules present. For AGS, the weight loss is much larger than that for AS (22%) for the entire temperature range when exposed to identical heating conditions. Between the temperature range (190–230 ℃), there is a weight loss of 14% which can be ascribed to the reduction of thermally less stable oxygenated functional groups on the silver/graphene oxide nanohybrid and/or complete decomposition of graphitic planes. The remaining solid residue above this temperature could be related to the silver content on the hybrid and may be the reason for greater stability of AGS.

The quantitative identification and elemental composition of AF and AGS were further analyzed by EDS (Fig. 7). The presence of carbon and oxygen in GO is clearly observable in the EDS spectrum of AF. In AGS elemental spectra, the peak corresponding to silver is spotted in addition to carbon and oxygen which demonstrates the successful loading of silver on partially reduced graphene oxide. The decreased oxygen content establishes the successful reduction of GO into partially reduced GO.

The surface composition of samples was examined using XPS. The wide scan spectrum of AGS given in Fig. 8 clearly shows the presence of C 1s, O 1s, Ag 3d, Ag 3p, Ag 4d, and Ag 4p peaks indicating the loading of silver on reduced graphene oxide. Information regarding the chemical state of carbon and silver species in the as-prepared samples is also provided by XPS spectra. Figure 9 shows XPS signature of silver metal—the Ag 3d doublet. The $Ag\ 3d_{3/2}$ and $Ag\ 3d_{5/2}$ of pure silver sample AS appear at binding energies 374.2 eV and 368.2 eV, respectively. These two peaks remarkably shift to lower energies at 373.07 eV and 367.07 eV for the nanohybrid AGS. This may be due to the electron transfer from AgNPs to partially reduced GO owing to the smaller work function of silver (4.2 eV) in comparison with that of graphene (4.48 eV) which might have occurred during the formation of the AGS [57]. The interaction between Ag and the carboxyl groups on the edge of graphene sheets also contributes to the electron transfer.
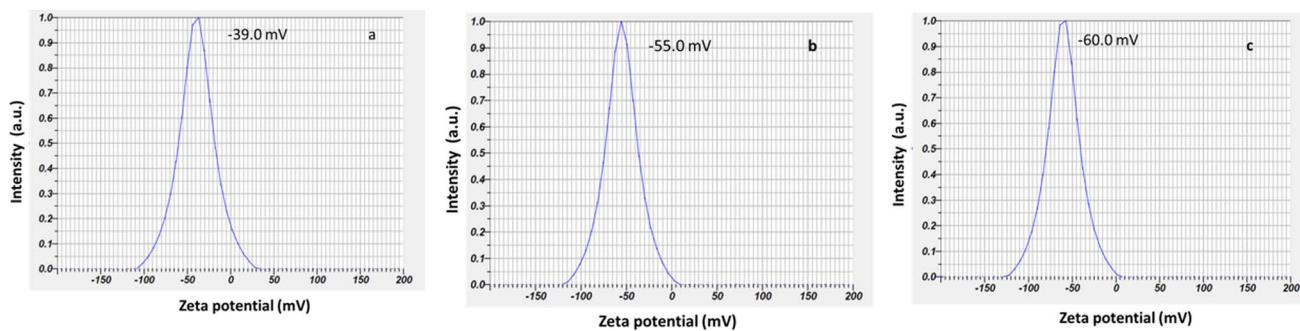
Fig. 5 Zeta potential of **a** graphene oxide, **b** silver nanoparticles, and **c** reduced graphene oxide–silver nanohybrid
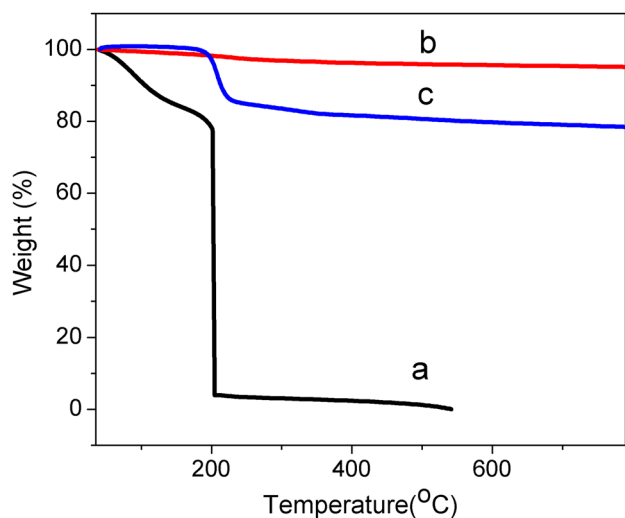

Fig. 6 TGA curve of **a** graphene oxide, **b** silver nanoparticles, and **c** reduced graphene oxide–silver nanohybrid

The binding energy of the higher ionic state of Ag is lower than that of zero-valent Ag which is attributed to the shifts in the initial-state potential of ionic charge and the lattice potential [72]. The slight oxidation on the surface of silver nanoparticles may be another reason for the negative shift of $Ag \ 3d_{3/2}$ and $Ag \ 3d_{5/2}$ binding energies [73]. Furthermore, the spin orbit splitting of the doublet components of Ag 3d is 6 eV which validates the formation of metallic silver in the hybrid nanomaterial AGS [74]. Figure 10 shows C1s XPS spectra of AF and AGS samples. For GO, this C 1 s spectra are deconvoluted into four peaks with binding energies 284.8 eV (C–C and or C=C), 285.4 eV (C=C and or C–OH), 286.9 eV (C–OH and or C–O–C), and 288.2 eV (HO–C=O) [75, 76]. This clearly indicates that GO is enriched with oxygen functional groups. As a consequence of close interaction between AgNPs and GO, the electronic properties of both samples get altered. From the deconvoluted C 1 s spectra of AGS, we can observe the absence/reduction in intensity
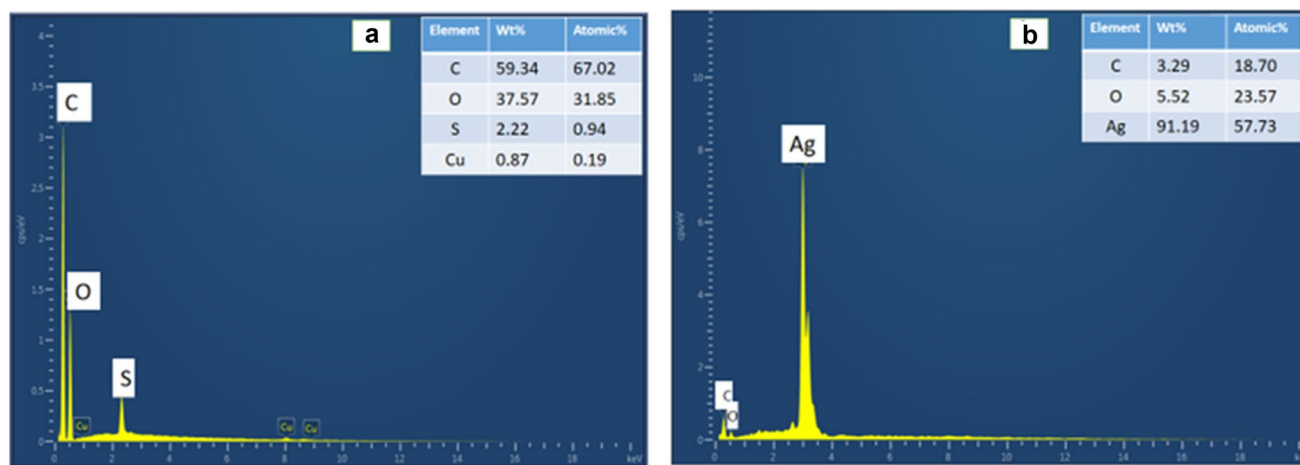

Fig. 7 EDS spectra of **a** graphene oxide and **b** reduced graphene oxide–silver nanohybrid
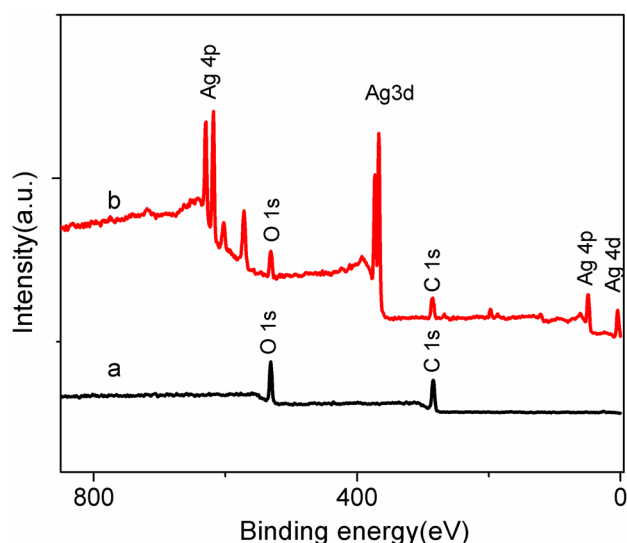
Fig. 8 Wide-scan XPS spectra of **a** graphene oxide and **b** reduced graphene oxide–silver nanohybrid

of some oxygenated functional peaks indicating the partial reduction of GO [56].

Based on nitrogen sorption measurements at 77 K, the Brunauer–Emmett–Teller (BET) surface areas of AS and AGS were investigated and the corresponding isotherms are depicted in Fig. 11 The BET surface area of sample AS is 5.7498 m^2/g, while for AGS, the value is 18.087 m^2/g. The increased value of AGS can be assigned to the incorporation of rGO which has a large surface area. Both samples exhibit a type IV isotherm with H3 hysteresis loop which indicates the formation of aggregates of plate-like particles forming slit-like pores [77, 78]. The small hysteresis loop of AS in the relative pressure (P/P_0) range of

0.85–1.0 is typically credited with the presence of textual mesopores [79, 80]. The addition of rGO shifts the hysteresis loop in the relative pressure (P/P_0) range to 0.4–1.0. Comparatively large hysteresis loop of AGS in this relative pressure (P/P_0) range is characteristic of the inhomogeneous hierarchically porous structure [81]. The nonlimiting adsorption for high relative pressure (P/P_0) > 0.9—characteristic of an H3 hysteresis loop indicates the presence of large meso- and macroporous materials [82].

Figure 12 shows the morphological characterization of the samples AF, AS, and AGS. The confirmation of the attachment of silver particles on reduced graphene oxide sheets are obtained from HRTEM studies. Almost transparent wrinkled sheet-like structure of GO is evident from the TEM image of AF (Fig. 12a), while that of silver nanoparticles presented in Fig. 12c indicates agglomerates of spherical or roughly spherical particles of sizes in the range 30–60 nm. Poly-dispersed silver particles in the range of 6–35 nm anchored to the silky wave surface of reduced graphene oxide are clearly observable in Fig. 12e. Of these, ultrafine silver particles (size < 10 nm) have spherical morphologies and an even homogeneous spreading on the rGO surface. The clean silky wavy nature of reduced graphene oxide sheets prevents the aggregation of rGO and facilitate the adherence of silver particles on rGO's surface. Selected area electron diffraction (SAED) pattern of AF (Fig. 12b) shows the polycrystalline nature of GO, while that of AS shown in Fig. 12d clearly indicates that the formation of nanoparticles is in crystalline nature [23]. Multiple crystal diffraction features of AGS are clearly evident in the SAED pattern given in Fig. 12f. Also the diffraction rings observed in background are due to rGO and bright spots correspond to the crystalline silver nanoparticles [83].
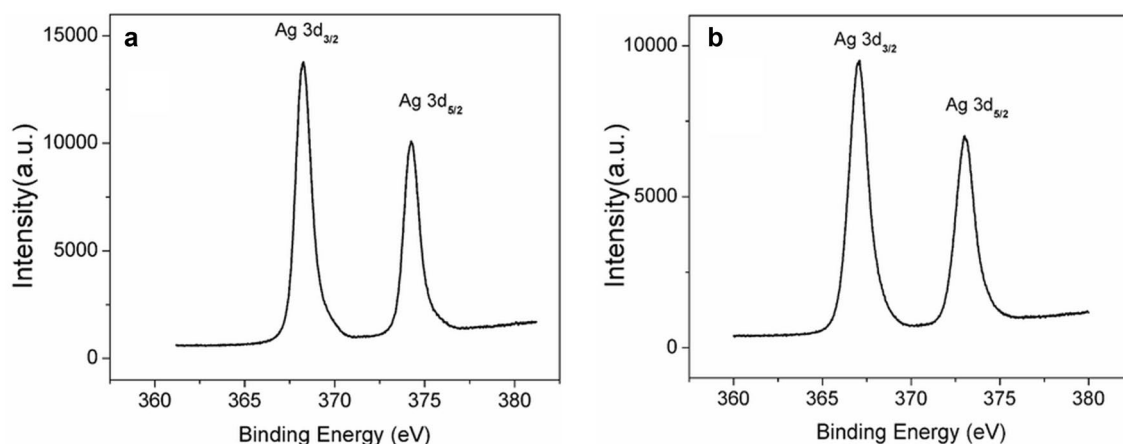

Fig. 9 XPS spectra of Ag 3d of **a** silver nanoparticles and **b** reduced graphene oxide–silver nanohybrid
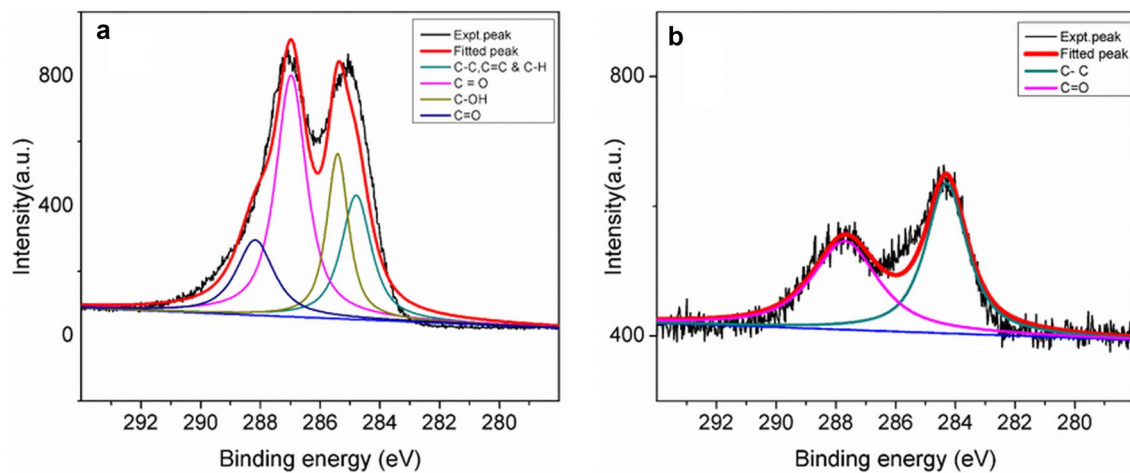
Fig. 10 XPS spectra of C 1 s of **a** graphene oxide and **b** reduced graphene oxide–silver nanohybrid
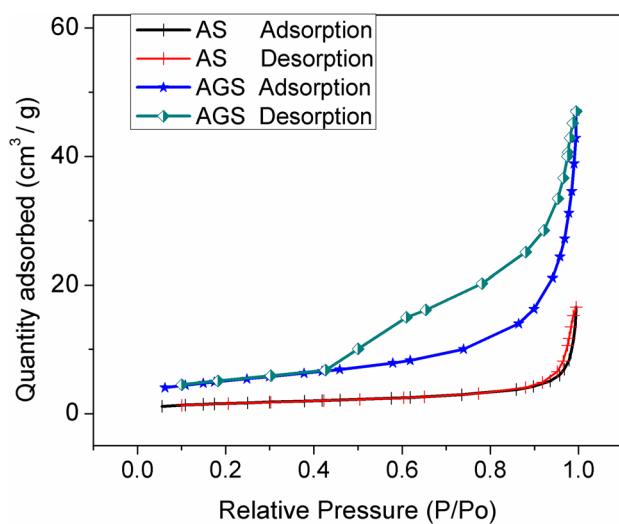

Fig. 11 N_2 adsorption–desorption isotherms of silver (AS) and reduced graphene oxide–silver nanohybrid (AGS)

3.2 Application as a biomaterial

3.2.1 Antibacterial activity: RMDA method

The RMDA method is carried out for finding the MIC value of the samples AF, AS, and AGS. In this antimicrobial susceptibility testing method, the twofold dilutions of the antimicrobial agent in a liquid growth medium are carried out using microtitration plates. Antibacterial activity of samples AF, AS, and AGS against two microorganisms *Escherichia coli* and *Bacillus subtilis* were investigated by this method. The experimental results are displayed in Fig. 13. C_1, C2, and C_3 represent the positive, negative, and broth control, respectively, while the samples AF, AS, and AGS are represented by A, B, and C.

All these experiments were performed in triplicate and the colour change was then assessed visually. The lowest concentration (average value) at which colour changed occurred from purple to pink was taken as the MIC value. As is clear from the tabulated results (Table 1), of the three samples, AGS showed a significant decrease in MIC value indicating total inhibition in growth of the bacteria—a decline in cellular viability. This phenomenon may be attributed to the synergistic antibacterial effect from both Ag and rGO. Exposure of silver nanoparticles to microorganisms causes adhesion of nanoparticles onto the cell wall. The bactericidal effect of these silver nanoparticles usually disrupts the bacterial cell membrane and damage intracellular structures which will lead to bacterial dysfunction and finally death [84]. The cell entrapment property of rGO ensures high local concentrations of Ag ions in the immediate vicinity of the cell membrane. At the same time, the physical interaction between the sharp edges of rGO sheets rupture the cell wall which enhances the transport of silver ions across it. It is also reported that the generation of reactive oxygen species (ROS) causes an increase in oxidative stress in cells and consequent cell death. AgNPS are associated with this ROS generation and the rGO sheets present in AGS could release silver ions slowly and will remain in stable structure for a relatively long time to generate ROS for bacteria inactivation [85, 86]. All these lead to the better antibacterial performance of AGS. Among the two bacterial strains evaluated, the Gram-positive bacteria *Bacillus subtilis* demonstrated the lowest MIC value in the presence of AGS nanohybrid. This may be due to the difference in the cellular wall structure between Gram-negative and Gram-positive bacteria and also due to the difference in the bactericidal activity of the nano hybrid which can be attributed to many different

Fig. 12 TEM images of **a** graphene oxide, **c** silver nanoparticles, **e** reduced graphene oxide-silver nanohybrid, and SAED pattern of **b** graphene oxide, **d** silver nanoparticles, and **f** reduced graphene oxide-silver nanohybrid
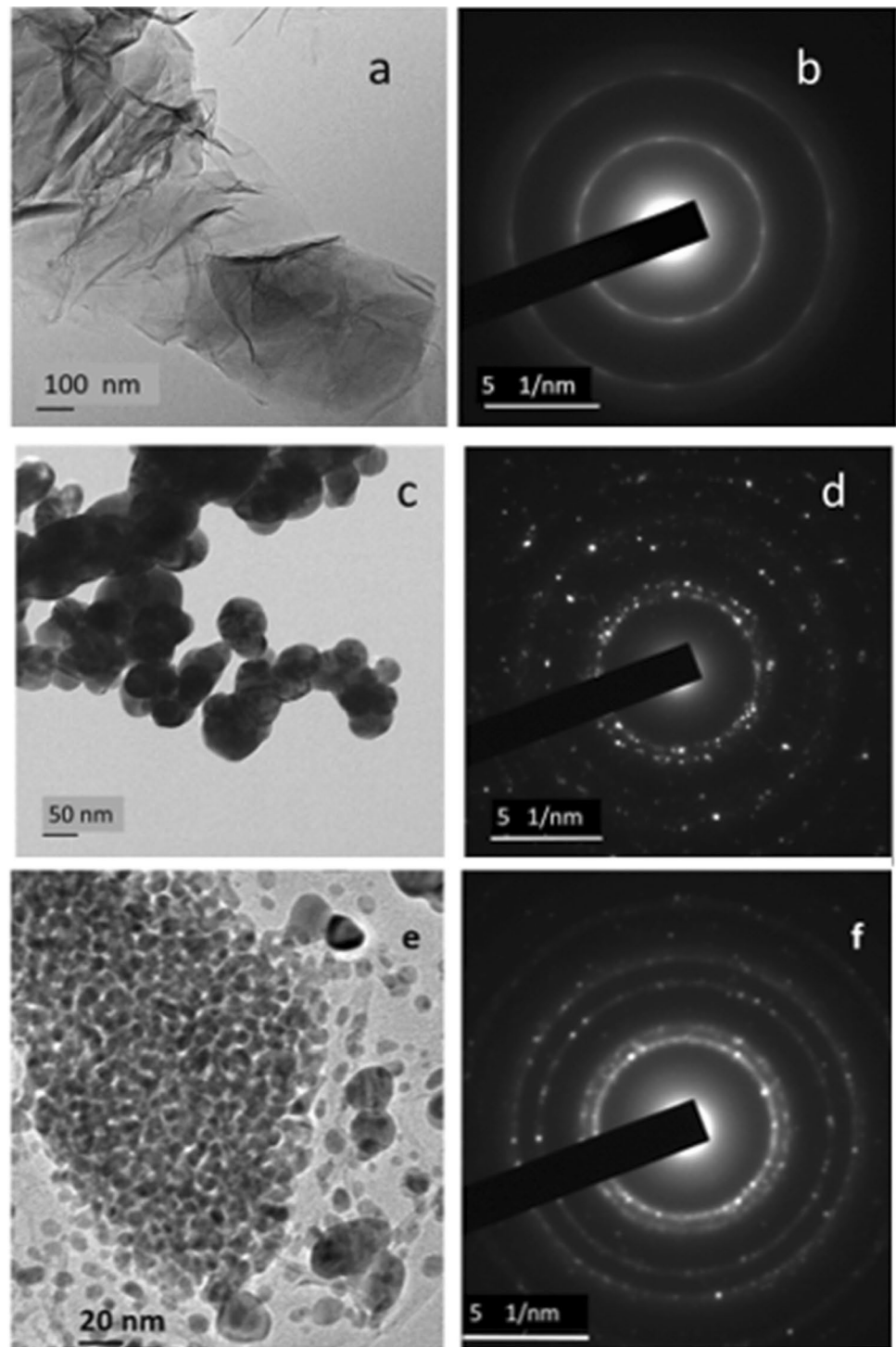
properties like ability to generate ROS [87]. Moreover, the MIC value of AGS for *Bacillus subtilis* was significantly lower than that presented by the conventional antibiotic Ampicillin, and for *Escherichia coli,* it is as good as the antibiotic. All these results support the potential application of rGO/Ag nanohybrid as an effective antimicrobial agent.
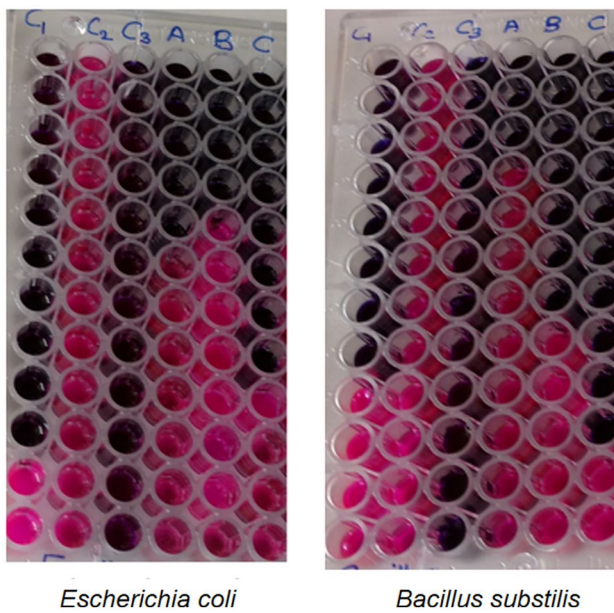
Fig. 13 MIC calculation of graphene oxide, silver nanoparticles, and reduced graphene oxide-silver nanohybrid against *Escherichia coli* and *Bacillus subtilis*: C1—positive control (ampicillin in serial dilution + broth + bacteria + indicator), C2—negative control (broth + bacteria + indicator), C3—broth control (broth + indicator); [A–C]—prepared samples (in serial dilution in wells 1–12 + broth + bacteria + indicator)

Fig. 14 Cytotoxicity analysis of DLA cells when treated with graphene oxide (AF), silver nanoparticles (AS), and reduced graphene oxide-silver nanohybrid (AGS)

3.2.2 Cytotoxicity study: trypan blue exclusion assay

Analyzing the effects of various materials on cell growth inhibition and/or cell death has been an important component of biological research. Trypan blue dye exclusion method is one of the methods used for this purpose and this method was employed to evaluate the short-term in vitro cytotoxicity of the as-prepared samples AGS, AS, and AF. The percentage cell death of the DLA cells at different concentrations of these nanomaterials ranging from 10 μg/mL to 200 μg/mL is studied and the results are shown in Fig. 14. The results demonstrate a dose-dependent inhibition of the growth of DLA cells with best results obtained for AGS at higher concentrations. The micrographs (Fig. 15) obtained when treated with the highest concentration of these materials indicate that the nanohybrid could be a potential agent in the area of cancer treatment. In these micrographs, dead cells appear as stained (blue) ones, because they have ruptured plasma membranes and cannot exclude trypan blue. At
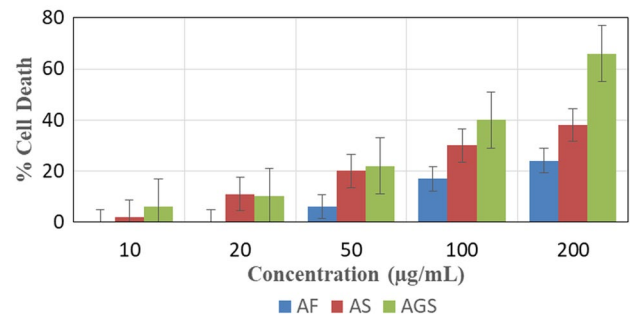
the same time, live cells have intact plasma membranes and they appear as unstained [49]. All these support our earlier assumption of the better capability shown by Ag/rGO nanohybrid in disrupting the cell membranes which exert a cytotoxic effect in tumour cells and inhibit tumour progression. Several previous studies already reported on the potential of GO and AgNP independently on inhibiting the cell viability in various types of cancer cells [15, 88, 89]. Reports suggest that the degree of toxicity of graphene family materials may vary due to a number of factors like the different carbon-to-oxygen ratio, chemical composition, charge transfer, presence of sharp edges, and the presence of functional groups [90]. The active physicochemical interaction of silver ions with the functional groups of intracellular proteins as well as with the nitrogen bases and phosphate groups in DNA is usually considered as the reason for the cytotoxic effect shown by AgNPs [91]. The synergistic interaction of both GO and AgNPs in a single platform may be the reason for the better performance of AGS. The rGO sheets decorated with AgNPs will prevent the aggregation of nanoparticles and hence allow the controlled release of $AgNP^+$ ions which eventually increase its cytotoxic performance [92].

3.2.3 Cytotoxicity study: MTT assay

To check the cytotoxicity in human cells, human colon epithelial carcinoma cells (HCT-15) were treated with test samples AS and AGS. The results obtained from the trypan blue assay method confirmed the trivial cytotoxic property of sample AF. Accordingly, we have not included AF in this study. The competence of the nanomaterials

Table 1 Minimum inhibitory concentrations of samples

Bacteria	Minimum inhibitory concentrations (mg/mL)			
	AF	AS	AGS	Ampicillin
Escherichia coli (ATCC 8739)	0.73 ± 0.48	0.52 ± 0.18	0.024 ± 0.02	0.02 ± 0.01
Bacillus subtilis (ATCC 11778)	1.04 ± 0.36	0.28 ± 0.29	0.019 ± 0.02	0.06 ± 0.04

AS and AGS as a potential inhibitory agent were probed using the MTT assay. The cytotoxicity of these nanomaterials was evaluated in a dose–response manner and the results are reported in Fig. 16. In addition, the half maximal inhibitory concentration, IC_{50} which is used to determine the lethal dosage of a substance in inhibiting biological functions was calculated. IC_{50} of AGS and AS on HCT-15 cell line were 42.73 µg/mL and 60.02 µg/mL

at 48 h, respectively. This shows that AGS possesses a more conspicuous anticancer capability and better inhibitory effect on cell viability than the other nanomaterial tested, AS. This might be due to the superior intracellular deliver properties of rGO, by which the cells are able to accumulate much more AgNPs when they are conjugated to rGO sheets and these particles are slowly released over long duration. Another reason for the high toxicity of AGS
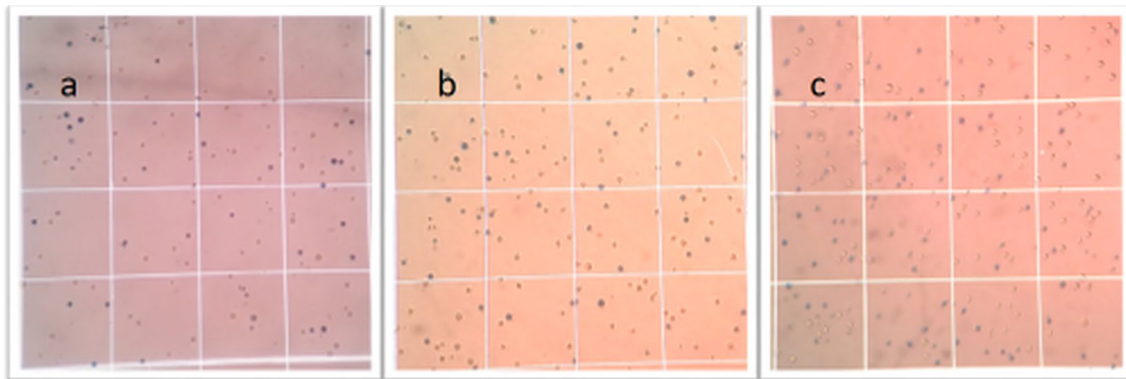

Fig. 15 Micrographs of DLA cells when treated with **a** graphene oxide, **b** silver nanoparticles, and **c** reduced graphene oxide–silver nanohybrid
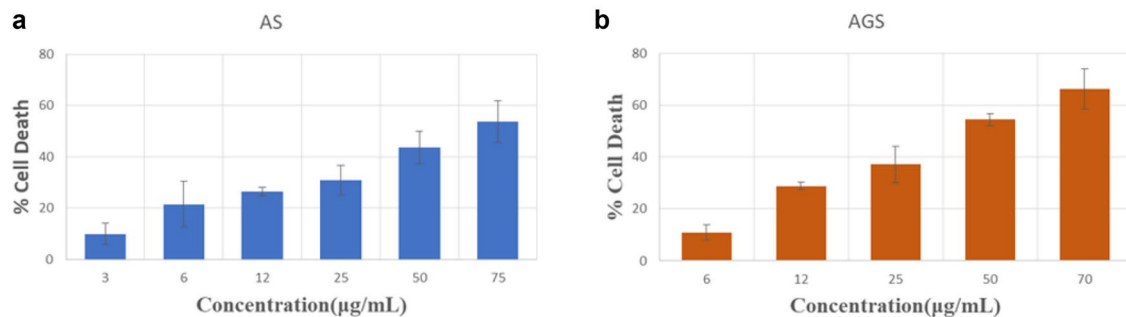

Fig. 16 Cytotoxicity analysis of HCT cells when treated with **a** silver nanoparticles (AS) and **b** reduced graphene oxide–silver nanohybrid (AGS)
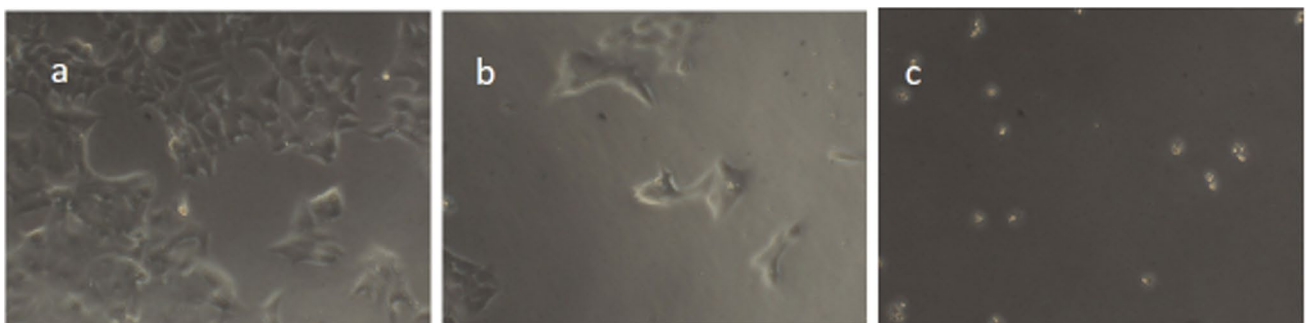

Fig. 17 Micrographs of **a** normal HCT cells, **b** when treated with 75 µg/mL silver nanoparticles, and **c** when treated with 50 µg/mL reduced graphene oxide–silver nanohybrid

is that metal-contaminated carbon products get more easily delivered to cells than other type of pure materials [93].

We further evaluated the effect of these nanomaterials on the cell morphology. Photomicrographs of the normal HCT cells and those of treated cancer cells with nanomaterials AGS and AS are given in Fig. 17. When treated with AS, reduced number of cells with a change on the cell morphology are observed. At the same time, AGS-treated cells appeared to be different from AS-treated cells. A substantial morphological change is observed between AGS-treated cells and normal ones. A high degree of cell growth inhibition is also observed in AGS-treated cells.

3.3 Application as an SERS substrate

The loading of irregular-shaped silver particles on the surface of rGO nanosheets produces a number of hot spots which make the hybrid material as a useful SERS substrate [94]. Figure 18 depicts the SERS spectra of 10^{-3} M RhB aqueous solution adsorbed on AS, AGS, and bare glass substrates. The spectra of the substrates show clearly the strong Raman active peaks of RhB molecules at 1205, 1279, 1358, 1507, and 1649 cm^{-1}, respectively, in good agreement with the literature reports [95, 96]. The signal observed at 1205 cm^{-1} is ascribed to aromatic C–H bending, while the peaks at 1358, 1507, and 1649 cm^{-1} are attributed to the C–C stretching of aromatic rings. The remaining one observed at 1279 cm^{-1} is assigned to C–C bridge band stretching. Throughout this work, we focus on 1649 cm^{-1} peak to characterize the Raman signal of RhB. It can be observed that the SERS intensity of as-prepared hybrid substrate AGS is substantially increased in comparison with

bare silver substrate AS. Furthermore, the SERS spectrum from AGS exhibits very sharp well-defined characteristic peaks revealing the high signal-to-noise ratio. This strong SERS activity may be attributed to the synchronic effects of silver particles and rGO. The rGO provides 2D platform with large surface area for the adsorption of AgNPs. These imbibed particles might have made the main contributions by the generation of more hotspots. The hotspot effect provides further enhancement in localized electromagnetic field which in turn may be caused by the localized surface plasmon resonance of metal nanostructures [97, 98]. Consequently, the D and G band intensities emanating from rGO in AGS are shielded and the characteristic peaks of RhB molecules are only observed [99].

Different concentrations of RhB were used to test the SERS sensitivity of the substrate AGS and the signature Raman peaks were still distinctive even at very low molar concentration. The Raman spectrum slightly shifts at lower concentrations (Fig. 19) which might be due to chemical enhancement mechanism [100]. To quantify the SERS activity of the substrate AGS, the enhancement factor (EF) was calculated using the formula:

$$EF = \left(\frac{I_{SERS}}{I_R} \right) \times \left(\frac{N_R}{N_{SERS}} \right), \tag{3}$$

where I_{SERS} and I_R are the intensities of the selected scattering bands in the SERS and bulk Raman spectra, respectively, N_{SERS} is the number of probe molecules contributing to the SERS signal, and N_R is the number of probe molecules contributing to the bulk Raman signal. Assuming that the
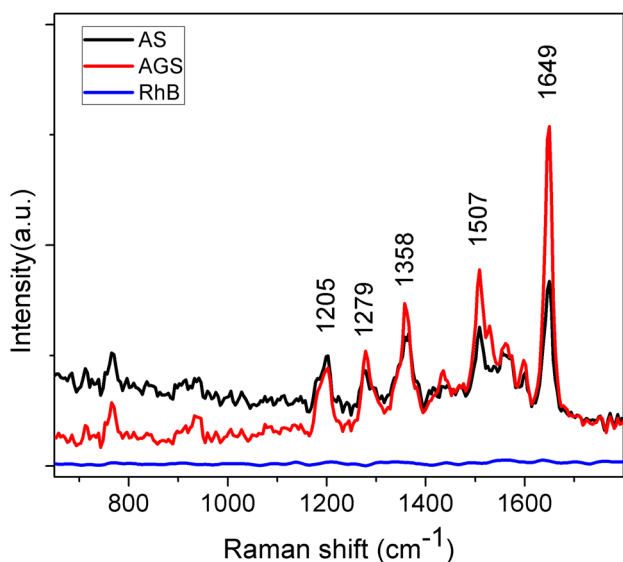

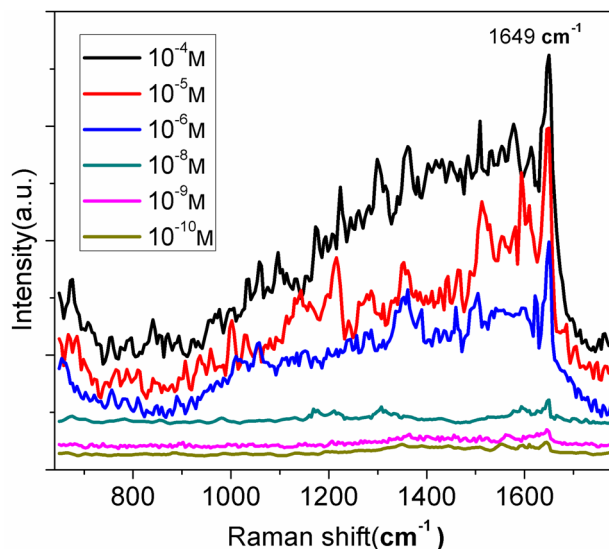**Fig. 18** SERS spectra of RhB (10^{-3} M) on substrates

Fig. 19 SERS spectra of different concentrations of RhB on reduced graphene oxide–silver nanohybrid substrate
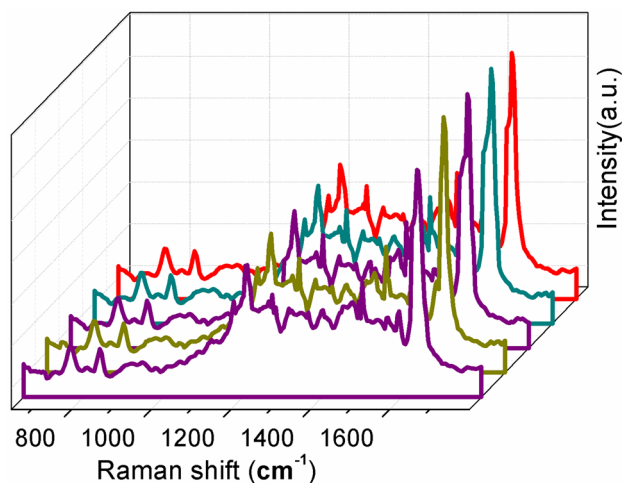
Fig. 20 SERS spectra of RhB at different positions on reduced graphene oxide–silver nanohybrid substrate

probed molecules are distributed on the substrates uniformly, the number of probe molecules contributing to the signal N can be estimated by:

$$N = N_A \times C \times V_{droplet} / A_{spot} \times A_{laser}, \tag{4}$$

where N_A is the Avogadro's number, C is the concentration of the used RhB, $V_{droplet}$ is the volume of the RhB droplet, A_{spot} is the area of the spot formed by the RhB droplet, and A_{laser} is the area of the laser spot. Since the substrates for SERS and bulk Raman tests are prepared in the same manner and measured with the same set of parameters, Eq. (3) can be written as:

$$EF = \left(\frac{I_{SERS}}{I_R} \right) \times \left(\frac{C_R}{C_{SERS}} \right), \tag{5}$$

where the subscripts R and SERS represent bulk Raman measurement and SERS measurement respectively [96, 101].

The peak intensity of 1649 cm^{-1} was chosen to calculate the EF of AGS for RhB molecules and it is approximately estimated to be 2.2×10^7.

To check the reproducibility and stability, SERS spectra (10^{-4} M) from five different positions on the substrate are collected under the same experimental conditions and are shown in Fig. 20. The relative standard deviation for the peak intensity at 1649 cm^{-1} is 5.3%, which confirms a good reproducibility over the whole area of the sample. The Raman spectra taken at different random points are nearly similar, the slight variations in intensity can be assigned to the non-uniform absorption of AgNPs on rGO surface.

The high EF value of this hybrid can be assigned to the synergistic effect between the AgNPs and the rGO sheets. Generally, there are two mechanisms to account for the SERS effect, chemical enhancement (CM), and electromagnetic enhancement (EM). The formation of more hot spots enhances the local electromagnetic field of AgNPs thus providing EM effect. The hot spots are formed mainly due to the surface plasmon resonance of AgNPs excited by the incident light [89]. CM effect and admirable adsorption properties to probe molecules introduced by the rGO sheets also contribute to higher value of EF [102]. The high surface area of the rGO sheets eases the charge transfer between the analyte and the substrate, and this provides the chemical enhancement.

4 Conclusions

In the current scenario of nanoscience, rGO/Ag nanohybrids are acquiring more and more attention due to its vast possibilities in various fields. Here, we have developed rGO/Ag nanohybrids as an effective SERS substrate with potentially active antibacterial, anticancerous properties. By optimizing this material with proper tuning of the load amount of silver particles on rGO surface, we can still improve its properties and can be explored for further potential applications. Since the use of SERS in biomedical and pharmaceutical research is rapidly growing, we hope that this hybrid material can further be developed, so that it finds wide application both as a drug and as a detection tool for biomolecules.

Compliance with ethical standards

Conflict of interest The authors declare that they have no conflict of interest.

References

1. V. Edwards-Jones, Lett. Appl. Microbiol. **49**, 147 (2009)
2. I. Chopra, J. Antimicrob. Chemother. **59**, 587 (2007)
3. H.J. Klasen, Burns **26**, 117 (2000)
4. W. Linlin, H. Chen, S. Longquan, Int. J. Nanomed. **12**, 1227 (2017)
5. A.C. Burduşel, O. Gherasim, A.M. Grumezescu, L. Mogoantă, A. Ficai, E. Andronescu, Nanomaterials **8**, 1 (2018)
6. N.R. Chowdhury, M. MacGregor-Ramiasa, P. Zilm, P. Majewski, K. Vasilev, J. Colloid Interface Sci. **482**, 151 (2016)
7. Y. Zhou, R.C. Tang, J. Photochem. Photobiol. B Biol. **178**, 463 (2018)
8. S. Prabhu, E.K. Poulose, Int. Nano Lett. **2**, 32 (2012)
9. S. Anandhakumar, V. Mahalakshmi, A.M. Raichur, Mater. Sci. Eng. C **32**, 2349 (2012)
10. C. Wan, J. Tai, J. Zhang, Y. Guo, Q. Zhu, D. Ling, F. Gu, J. Gan, C. Zhu, Y. Wang, S. Liu, F. Wei, Q. Cai, Cell Death Dis. **10** (2019)

11. R. Foulkes, M. Ali Asgari, A. Curtis, C. Hoskins, ACS Appl. Nano Mater. **2**, 1758 (2019)
12. P. Karuppaiya, E. Satheeshkumar, H.S. Tsay, Mol. Biol. Rep. **46**, 4725 (2019)
13. J. Venkatesan, S. Kim, M. Shim, Nanomaterials **6**, 235 (2016)
14. M. Buttacavoli, N.N. Albanese, G. Di Cara, R. Alduina, C. Faleri, M. Gallo, G. Pizzolanti, G. Gallo, S. Feo, F. Baldi, P. Cancemi, Oncotarget **9**, 9685 (2018)
15. K. Vasanth, K. Ilango, R. MohanKumar, A. Agrawal, G.P. Dubey, Colloids Surf. B Biointerfaces **117**, 354 (2014)
16. R.M. Gengan, K. Anand, A. Phulukdaree, A. Chuturgoon, Colloids Surf. B Biointerfaces **105**, 87 (2013)
17. A.A. Kajani, S.H. Zarkesh-Esfahani, A.K. Bordbar, A.R. Khosropour, A. Razmjou, M. Kardi, J. Mol. Liq. **223**, 549 (2016)
18. V. De Matteis, M. Cascione, C.C. Toma, S. Leporatti, Nanomaterials **8** (2018)
19. T.K. Naqvi, A.K. Srivastava, M.M. Kulkarni, A.M. Siddiqui, P.K. Dwivedi, Appl. Surf. Sci. **478**, 887 (2019)
20. P. Mosier-Boss, Nanomaterials **7**, 142 (2017)
21. Z.L. Taixing Tan, C. Tian, Z. Ren, J. Yang, Y. Chen, L. Sun, J.Y., H. F. Aiping Wu, Phys.Chem. Chem. Phys **15**, 21034 (2013)
22. Z. Zhang, K. Bando, K. Mochizuki, A. Taguchi, K. Fujita, S. Kawata, Anal. Chem. **91**, 3254 (2019)
23. W. Shao, X. Liu, H. Min, G. Dong, Q. Feng, S. Zuo, A.C.S. Appl. Mater. Interfaces **7**, 6966 (2015)
24. S. Kulshrestha, S. Qayyum, A.U. Khan, Microb. Pathog. **103**, 167 (2017)
25. S.W. Chook, C.H. Chia, S. Zakaria, M.K. Ayob, K.L. Chee, N.M. Huang, H.M. Neoh, H.N. Lim, R. Jamal, R.M.F.R.A. Rahman, Nanoscale Res. Lett. **7**, 1 (2012)
26. P. Paik, J. Nanomed. Res. **5** (2017)
27. M.Y. Xia, Y. Xie, C.H. Yu, G.Y. Chen, Y.H. Li, T. Zhang, Q. Peng, J. Control. Rel. **307**, 16 (2019)
28. A.C.M. de Moraes, B.A. Lima, A.F. de Faria, M. Brocchi, O.L. Alves, Int. J. Nanomed. **10**, 6847 (2015)
29. S. Liu, T.H. Zeng, M. Hofmann, E. Burcombe, J. Wei, R. Jiang, J. Kong, Y. Chen, ACS Nano **5**, 6971 (2011)
30. I. Barbolina, C.R. Woods, N. Lozano, K. Kostarelos, K. S. Novoselov, I.S. Roberts, 2D Mater. **3**, 1 (2016)
31. M. Sawangphruk, P. Srimuk, P. Chiochan, T. Sangsri, P. Siwayaprahm, Carbon N. Y. **50**, 5156 (2012)
32. J.A. Jaleel, S. Sruthi, K. Pramod, J. Control. Rel. **255**, 218 (2017)
33. J. Liu, J. Dong, T. Zhang, Q. Peng, J. Control. Rel. **286**, 64 (2018)
34. X. Xu, X. Tang, X. Wu, X. Feng, J. Photochem. Photobiol. B Biol. **191**, 1 (2019)
35. T.T. Pham, H.T. Nguyen, C.D. Phung, S. Pathak, S. Regmi, D.H. Ha, J.O. Kim, C.S. Yong, S.K. Kim, J.E. Choi, S. Yook, J.B. Park, J.H. Jeong, J. Ind. Eng. Chem. **76**, 310 (2019)
36. S. He, K. Liu, S. Su, J. Yan, X. Mao, D. Wang, Y. He, L. Li, S. Song, C. Fan, Anal. Chem. **84**, 4622 (2012)
37. L. Ouyang, L. Yao, T. Zhou, L. Zhu, Anal. Chim. Acta **1027**, 83 (2018)
38. X. Li, J. Chem. **2018**, 1 (2018)
39. P. Karthick Kannan, P. Shankar, C. Blackman, C.H. Chung, Adv. Mater (2019)
40. D. Cialla, S. Pollok, C. Steinbrücker, K. Weber, J. Popp, Nanophotonics **3**, 383 (2014)
41. D.C. Marcano, D.V. Kosynkin, J.M. Berlin, A. Sinitskii, Z. Sun, A. Slesarev, L.B. Alemany, W. Lu, J.M. Tour, ACS Nano **4**, 4806 (2010)
42. M.R. Das, R.K. Sarma, S.C. Borah, R. Kumari, R. Saikia, A.B. Deshmukh, M.V. Shelke, P. Sengupta, S. Szunerits, R. Boukherroub, Colloids Surf. B Biointerfaces **105**, 128 (2013)
43. M. Moghayedi, E.K. Goharshadi, K. Ghazvini, H. Ahmadzadeh, L. Ranjbaran, R. Masoudi, R. Ludwig, Colloids Surf. B Biointerfaces **159**, 366 (2017)
44. M. Balouiri, M. Sadiki, S.K. Ibnsouda, J. Pharm. Anal. **6**, 71 (2016)
45. S.D. Sarker, L. Nahar, Y. Kumarasamy, Methods **42**, 321 (2007)
46. F. Palomino, J.C. Martin, A. Camacho, M. Guerra, H. Swings, J. Portaels, Antimicrob. Agents Chemother. **46**, 2720 (2002)
47. W. Strober, Curr. Protoc. Immunol. **111**, 1 (2015)
48. T. Mosmann, J Immunol Methods. **65**, 55 (1983)
49. L.C. Crowley, B.J. Marfell, M.E. Christensen, N.J. Waterhouse, Cold Spring Harb. Protoc. **2016**, 643 (2016)
50. P. Chamoli, M.K. Das, K.K. Kar, Phys. E Low Dimens. Syst. Nanostruct. **90**, 76 (2017)
51. S. Park, J. An, I. Jung, R.D. Piner, S.J. An, X. Li, A. Velamakanni, R.S. Ruoff, Nano Lett. **9**, 1593 (2009)
52. N. Díez, A. Śliwak, S. Gryglewicz, B. Grzyb, G. Gryglewicz, RSC Adv. **5**, 81831 (2015)
53. C. Xu, X. Wang, Small **5**, 2212 (2009)
54. S. Chen, J. Zhu, X. Wu, Q. Han, X. Wang, ACS Nano **4**, 2822 (2010)
55. A. Soroush, W. Ma, Y. Silvino, M.S. Rahaman, Environ. Sci. NANO **2**, 395 (2015)
56. J. Li, C.Y. Liu, Eur. J. Inorg. Chem. 1244 (2010)
57. V. Bansal, V. Li, A.P. O'Mullane, S.K. Bhargava, CrystEngComm **12**, 4280 (2010)
58. V.H. Nguyen, B.K. Kim, Y.L. Jo, J.J. Shim, J. Supercrit. Fluids **72**, 28 (2012)
59. K. Krishnamoorthy, M. Veerapandian, K. Yun, S.J. Kim, Carbon N. Y. **53**, 38 (2013)
60. Y.G. Yuan, S. Gurunathan, Int. J. Nanomed. **12**, 6537 (2017)
61. D. Konios, M.M. Stylianakis, E. Stratakis, E. Kymakis, J. Colloid Interface Sci. **430**, 108 (2014)
62. D. Graf, F. Molitor, K. Ensslin, C. Stampfer, A. Jungen, C. Hierold, L. Wirtz, Nano Lett. **7**, 238 (2007)
63. Y. Xiao, J. Liu, Y. Lin, W. Lin, Y. Fang, J. Alloys Compd. **698**, 170 (2017)
64. M.A. Pimenta, G. Dresselhaus, M.S. Dresselhaus, L.G. Cançado, A. Jorio, R. Saito, Phys. Chem. Chem. Phys. **9**, 1276 (2007)
65. S. Fathalipour, E. Abdi, Synth. Met. **221**, 159 (2016)
66. E.Ç. Salihi, J. Wang, D.J.L. Coleman, L. Šiller, Sep. Sci. Technol. **51**, 1317 (2016)
67. I. Roy, D. Rana, G. Sarkar, A. Bhattacharyya, N.R. Saha, S. Mondal, S. Pattanayak, S. Chattopadhyay, D. Chattopadhyay, RSC Adv. **5**, 25357 (2015)
68. K.H. Tseng, H.C. Ku, D.C. Tien, L. Stobinski, Nanomaterials **9** (2019)
69. Y. Liu, Y. Zhang, T. Zhang, Carbon N. Y. **71**, 166 (2014)
70. C. Zhu, S. Guo, Y. Fang, S. Dong, ACS Nano **4**, 2429 (2010)
71. A.R. Kumarasinghe, L. Samaranayake, F. Bondino, E. Magnano, N. Kottegoda, E. Carlino, U.N. Ratnayake, A.A.P. De Alwis, V. Karunaratne, G.A.J. Amaratunga, J. Phys. Chem. C **117**, 9507 (2013)
72. L. He, S.C. Tjong, RSC Adv. **7**, 2058 (2017)
73. S. Cui, S. Mao, Z. Wen, J. Chang, Y. Zhang, J. Chen, Analyst **138**, 2877 (2013)
74. H. Ma, J. Zeng, S. Harrington, L. Ma, M. Ma, X. Guo, Y. Ma, Nanomaterials **6**, 1 (2016)
75. J. Zeng, X. Tian, J. Song, Z. Wei, S. Harrington, Y. Yao, L. Ma, Y. Ma, J. Mater. Sci. Mater. Electron. **27**, 3540 (2016)
76. X.Z. Tang, X. Li, Z. Cao, J. Yang, H. Wang, X. Pu, Z.Z. Yu, Carbon N. Y. **59**, 93 (2013)
77. Y. Gao, Y. Zhao, G. Zhang, L. Deng, J. Li, R. Sun, L. Li, C.P. Wong, J. Mater. Sci. **50**, 3399 (2015)
78. K.S.W. Sing, Pure Appl. Chem. **57**, 603 (1985)
79. S.M. Hosseini, H. Hosseini-Monfared, V. Abbasi, M.R. Khoshroo, Inorg. Chem. Commun. **67**, 72 (2016)
80. S. Zhang, S. Gai, F. He, S. Ding, L. Li, P. Yang, Nanoscale **6**, 11181 (2014)

81. D.A. Reddy, J. Choi, S. Lee, R. Ma, T.K. Kim, RSC Adv. **5**, 67394 (2015)

82. C.J. Cai, M.W. Xu, S.J. Bao, C.C. Ji, Z.J. Lu, D.Z. Jia, Nanotechnology **24**, 275602 (2013)

83. H. Wadhwa, D. Kumar, S. Mahendia, S. Kumar, Mater. Chem. Phys. **194**, 274 (2017)

84. Y. Qing, L. Cheng, R. Li, G. Liu, Y. Zhang, X. Tang, J. Wang, H. Liu, Y. Qin, Int. J. Nanomed. **13**, 3311 (2018)

85. Z. Yang, X. Hao, S. Chen, Z. Ma, W. Wang, C. Wang, L. Yue, H. Sun, Q. Shao, V. Murugadoss, Z. Guo, J. Colloid Interface Sci. **533**, 13 (2019)

86. K. Prasad, G.S. Lekshmi, K. Ostrikov, V. Lussini, J. Blinco, M. Mohandas, K. Vasilev, S. Bottle, K. Bazaka, K. Ostrikov, Sci. Rep. **7** (2017)

87. Y.N. Slavin, J. Asnis, U.O. Häfeli, H. Bach, J. Nanobiotechnol. **15**, 1 (2017)

88. S. Wu, X. Zhao, Z. Cui, C. Zhao, Y. Wang, L. Du, Y. Li, Int. J. Nanomed. **9**, 1413 (2014)

89. S. Gurunathan, M. Kang, M. Jeyaraj, J. Kim, Nanomaterials **9**, 1 (2019)

90. S. Gurunathan, M. Kang, M. Jeyaraj, J. Kim, Int. J. Mol. Sci. **20**, 1 (2019)

91. M.I. Sriram, S.B.M. Kanth, K. Kalishwaralal, S. Gurunathan, Int. J. Nanomed. **5**, 753 (2010)

92. Y.G. Yuan, Y.H. Wang, H.H. Xing, S. Gurunathan, Int. J. Nanomed. **12**, 5819 (2017)

93. F. Shaheen, M. Hammad Aziz, M. Fakhar-e-Alam, M. Atif, M. Fatima, R. Ahmad, A. Hanif, S. Anwar, F. Zafar, G. Abbas, S. Ali, M. Ahmed, Nanomaterials **7**, 401 (2017)

94. Z. Zhang, F. Xu, W. Yang, M. Guo, X. Wang, B. Zhang, J. Tang, Chem. Commun. **47**, 6440 (2011)

95. J. Zhang, X. Li, X. Sun, Y. Li, J. Phys. Chem. B **109**, 12544 (2005)

96. X. Liu, Y. Shao, Y. Tang, K.F. Yao, Sci. Rep. **4**, 1 (2014)

97. X. Yu, J. Tao, Y. Shen, G. Liang, T. Liu, Y. Zhang, Q.J. Wang, Nanoscale **6**, 9925 (2014)

98. A.K. Nair, K.B. Bhavitha, S. Perumbilavil, P. Sankar, D. Rouxel, M.S. Kala, S. Thomas, N. Kalarikkal, Carbon N. Y. **132**, 380 (2018)

99. Y. Li, X. Zhao, P. Zhang, J. Ning, J. Li, Z. Su, G. Wei, J. Mater. Chem. C **3**, 4126 (2015)

100. C.H. Sun, M.L. Wang, Q. Feng, W. Liu, C.X. Xu, Russ. J. Phys. Chem. A **89**, 291 (2015)

101. Y. Xie, Y. Meng, RSC Adv. **4**, 41734 (2014)

102. X. Zhao, J. Yu, C. Zhang, C. Chen, S. Xu, C. Li, Z. Li, S. Zhang, A. Liu, B. Man, Appl. Surf. Sci. **455**, 1171 (2018)